



Reprinted from JOURNAL OF THE ELECTROCHEMICAL SOCIETY
Vol. 132, No. 2, February 1985
Printed in U.S.A.
Copyright 1985

High Field Phenomena in Thermal SiO₂

C. Glenn Shirley¹

Motorola, Incorporated, Process Technology Laboratory, SRDL, Phoenix, Arizona 85008

ABSTRACT

High field phenomena in thermally grown SiO₂ have been investigated by a combination of three techniques: (i) current-voltage characterization, (ii) CV measurements, and (iii) forced-current voltage-time characteristics. Comparison with theoretical Fowler-Nordheim predictions was used in the current-voltage technique. Four oxide thicknesses were studied: 160, 345, 652, and 1452 Å. All structures were nonrecessed Al/SiO₂/Si capacitors of various areas. The substrate was n-type silicon. Interface trap formation and charging with electrons near the cathode during injection from Si was observed for all oxides. Creation of immobile holes in the oxide valence band by impact ionization was observed for the thicker oxides, but not the thinnest. Bulk trapping was significant when electrons were injected from Al into the thicker oxides. The Al/SiO₂ interface was considerably leakier in thicker oxides than predicted by the Fowler-Nordheim theory. It is important to consider these high field phenomena in reliability questions because they constitute a true wear-out mechanism for intrinsic (i.e., with no defects) thermal oxides. As oxides become thinner in devices, high field phenomena become a more practical concern.

As integrated circuits shrink, thinner thermal oxides of silicon are required to withstand higher electric fields. This is beginning to change the situation with regard to oxide reliability. Historically, oxide reliability has been limited by defects which have early breakdown characteristics. Much has been done to predict and minimize defect-related failure rates. Statistical methods have played a large role in this. A common procedure is to screen devices by applying a high voltage during an accelerated test. The surviving population has a large reduction in early failure rate at the cost of a small loss in manufacturing yield. This rationale does not apply if oxides fail by a true wear-out mechanism. This is because accelerated stress weakens the entire population. The thin oxides used in VLSI processing must be more nearly defect-free because they must withstand higher fields. Thus, increasingly, reliability is being limited not by defects but by the intrinsic high field processes we shall be examining in this report. The main problem is not that devices will suffer wear-out in operation, but that the likelihood of stressing devices into wear-out during the accelerated testing used to screen devices. Hence the importance of studying the high field behavior of thermal oxides.

The purpose of this paper is to review intrinsic high field phenomena in thermal oxides and to demonstrate

how they may be observed. With this report as a guide, we are in a good position to characterize quickly the high field behavior of any gate oxide system (silicides, etc.).

In this study, three kinds of data were acquired: (i) IV data, (ii) CV data, and (iii) the V-t characteristics obtained when a constant current is forced through the MOS capacitor. All three types of data were gathered as function of capacitor area and oxide thickness. No area dependence beyond simple scaling of current and capacitance with area was found. That is, edge effects were negligible. The study was carried out on the Al/SiO₂/n-type Si system.

Theoretical Background

Figure 1 shows a schematic of the well-known (1, 2) band structure of the Al/SiO₂/Si MOS diode. Electrons in Si or Al have high potential barriers at the interface to surmount before they can enter the SiO₂. As the potential difference across the oxide is increased, the barrier at the negative (electron injecting) electrode becomes sharply triangular. When the barrier thickness, d , at the Fermi level of the injecting electrode becomes of the order of 50 Å, appreciable numbers of electrons can enter the oxide conduction band by quantum tunneling through the interfacial barrier. By simple trigonometry, this occurs at an electric field of about $\phi_{si}/d \approx 3.0 \text{ eV}/50 \times 10^{-8} \text{ cm} \approx 6 \times$

¹Present address: Intel Corporation, Chandler, Arizona 85224.

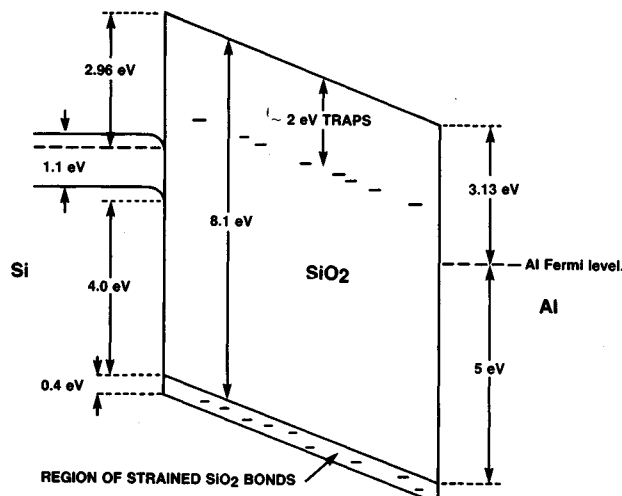


Fig. 1. Band diagram of Si/SiO₂/Al system shown with aluminum biased positive relative to silicon.

10^6 V/cm. The barrier height for electrons at the Si/SiO₂ interface is denoted by ϕ_{Si} . Once in the conduction band of the oxide, the electrons have high mobility [20-40 cm²/V-s, Ref. (1)] and move rapidly to the anode. Some electrons may fall into the fairly numerous traps at about 2 eV below the oxide conduction band, but they will immediately tunnel out of them at the high electric fields necessary to cause injection from the cathode. Holes injected from the anode have a much higher barrier (4-5 eV) to surmount than electrons, and holes are known to have a very low mobility in the oxide [2×10^{-5} cm²/V-s, Ref. (1)]. The low hole mobility is probably due to the large number of shallow hole traps just above the valence band of SiO₂ due to strained Si-O bonds. Hence, the number of injected holes and their influence on conduction is negligible in our experiments. Hot holes can be injected into SiO₂ by avalanche injection from n-type silicon driven into deep depletion, but this condition does not occur in our experiments.

When a constant current is forced into a MOS capacitor, the leakage current-voltage-time characteristic appears as shown schematically in Fig. 2. The leakage current is the forced current less the displacement current. The displacement current can be calculated from $I(\text{disp}) = C(dV/dt)$ where C is the capacitance of the MOS capacitor and dV/dt is the instantaneous rate of increase in voltage. The IV characteristic of the oxide is shown as a projec-

Table I. Oxide thickness measured by IBM thin film analyzer

Wafer no.	Thickness (Å)
5	144 (160 ^a)
6	345
7	652
8	1452

^a Better agreement between theory and experiment for IV data was obtained with $t_{ox} = 160\text{\AA}$.

tion on the IV plane, while the V-t characteristic obtained when a constant current is forced is shown as a projection on the V-t plane. Figure 2 summarizes the various regimes of importance in the electrical behavior of thermal oxide. At low electric fields, no charge is injected from the electrodes, but electrons will be ejected from shallow traps and will flow to the anode. This is the origin of the flat part of the IV curve labeled "trap emptying." We will not be examining this regime in this report, but we indicate in passing that techniques measuring trap filling and emptying transients at low fields can be used to gauge oxide quality. At higher electric fields, quantum tunneling at the electron injecting electrode (cathode) becomes dominant and the IV characteristic follows the Fowler-Nordheim (FN) law (3-5) (labeled "FN conduction" in Fig. 2). The FN characteristic can be extended to lower fields by maintaining a bias in the trap emptying regime to drain the shallow traps before taking the FN trace. This "uncovers" the FN characteristic at lower fields (4). At high fields, just prior to breakdown, the IV characteristic deviates from the FN law in a time-dependent fashion (4-6) labeled "high-field prebreakdown" in Fig. 2. It is important to realize that the measured injected current depends on the local electric field in the oxide at the cathode. This is the same as the average field across the oxide only if there is no charge in the dielectric. The average field is what is experimentally measured. Therefore, the high field deviations from the FN law are due to charging in the oxide. The charges take time to build up. Hence, the high field deviations from the FN law are time dependent. These charges are intimately related to the intrinsic (that is, nondefect-related) breakdown mechanism. This report is about the FN conduction regime, and the high field prebreakdown regime and the time dependence of the latter. This report does not consider the yield issues associated with defect-caused breakdowns. While this is of great importance, our focus is on the intrinsic properties of the oxide.

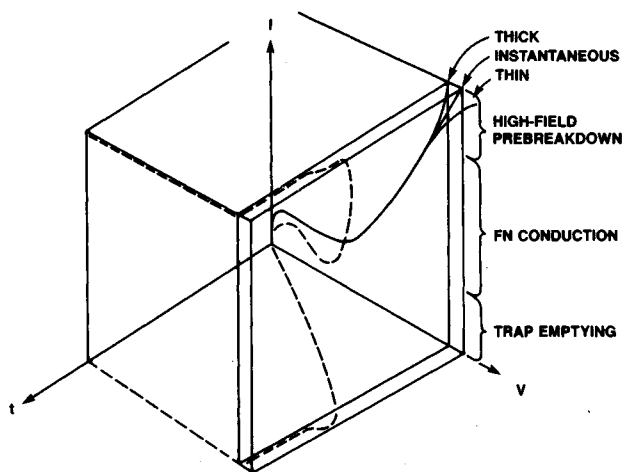


Fig. 2. Schematic of leakage current-voltage-time characteristic. At high fields, the IV characteristic changes with time as charge builds up in the oxide. The time-dependent deviation from the ideal Fowler-Nordheim law at high fields depends on oxide thickness.

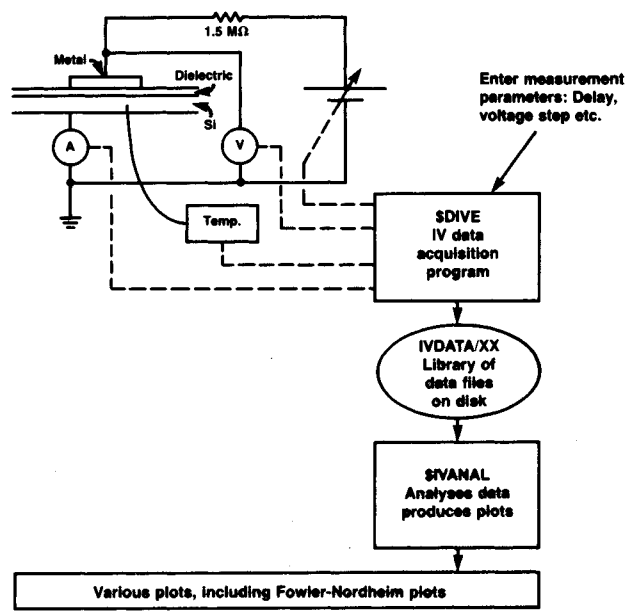


Fig. 3. Computer-automated IV data acquisition and analysis system

Sample Preparation

Four <100> n-type phosphorous-doped wafers with $N = 5 \times 10^{14} \text{ cm}^{-3}$ were separately thermally oxidized using a standard HCl cycle. Only the time in the growth part of the cycle was varied to change the thicknesses of the oxides. The oxide thicknesses were measured using an IBM Film Thickness Analyzer (FTA). The thicknesses obtained are shown in Table I. We shall see later that better agreement between theory and experiment for the IV data of wafer 5 was obtained if the thickness of the thinnest oxide is taken to be 160 Å rather than the 144 Å given by the IBM FTA. Much of the data analysis will use 160 Å instead of 144 Å. This is a reasonable correction, since the IBM FTA gives estimates consistently lower than other thickness measurement techniques such as ellipsometry, CV, etc. Next, 1000 Å of aluminum was deposited on the wafers and then patterned into arrays of rectangular capacitors of various areas. The wafers were then annealed at 450°C for 30 min in forming gas. Finally, the oxide was stripped from the backs of the wafers using an HF fume. All wafers were processed identically except for the growth part of the oxidation cycle.

Electrical Measurements

Current-voltage measurements.—Current-voltage characteristics were measured using the system shown in Fig. 3. A Tektronix 4051 computer controls a Kepco BOP500M bipolar power supply with 500V range. The current flowing from the chuck to ground is monitored by a Keithley 616 electrometer and transmitted to the computer by a

custom interface built in our laboratory. The voltage on the probe is measured by a Fluke 8502A digital multimeter and transmitted to the computer via the general purpose interface bus (GPIB). There is also provision for heating or cooling the sample under computer control, but this was not used in these experiments. All measurements were done at room temperature. The program \$DIVE controls the instruments and acquires the data. The voltage applied to a MOS capacitor was increased in approximately 1V steps until electrical breakdown of the oxide occurred. A 4s delay after each voltage step allowed displacement current transients to decay. IV characteristics were obtained in this way on 25 and 625 mil² capacitors in both positive and negative polarities. Each characteristic was obtained on a virgin capacitor, and measurements for any given set of conditions were repeated on virgin capacitors to ensure reproducibility.

Once the data were acquired, they were saved in a library of data files, IVDATA (Fig. 3), on a floppy disk reserved for data. Also saved are an identifying string, the area of the capacitor and the thickness of the oxide. These files can be read by the program \$IVANAL and various types of plots can be generated. Of particular importance in this study are Fowler-Nordheim (FN) plots: $\log(J/E^2)$ vs. $1/E$, where J is the current density and E is the average field across the dielectric (*i.e.*, $E = \text{total voltage drop}/\text{oxide thickness}$). The FN plots for 25 mil² capacitors for four oxide thicknesses in both polarities are shown in Fig. 4 and 5. The plotting program ignores the sign of the voltage drop across the oxide except that data taken with

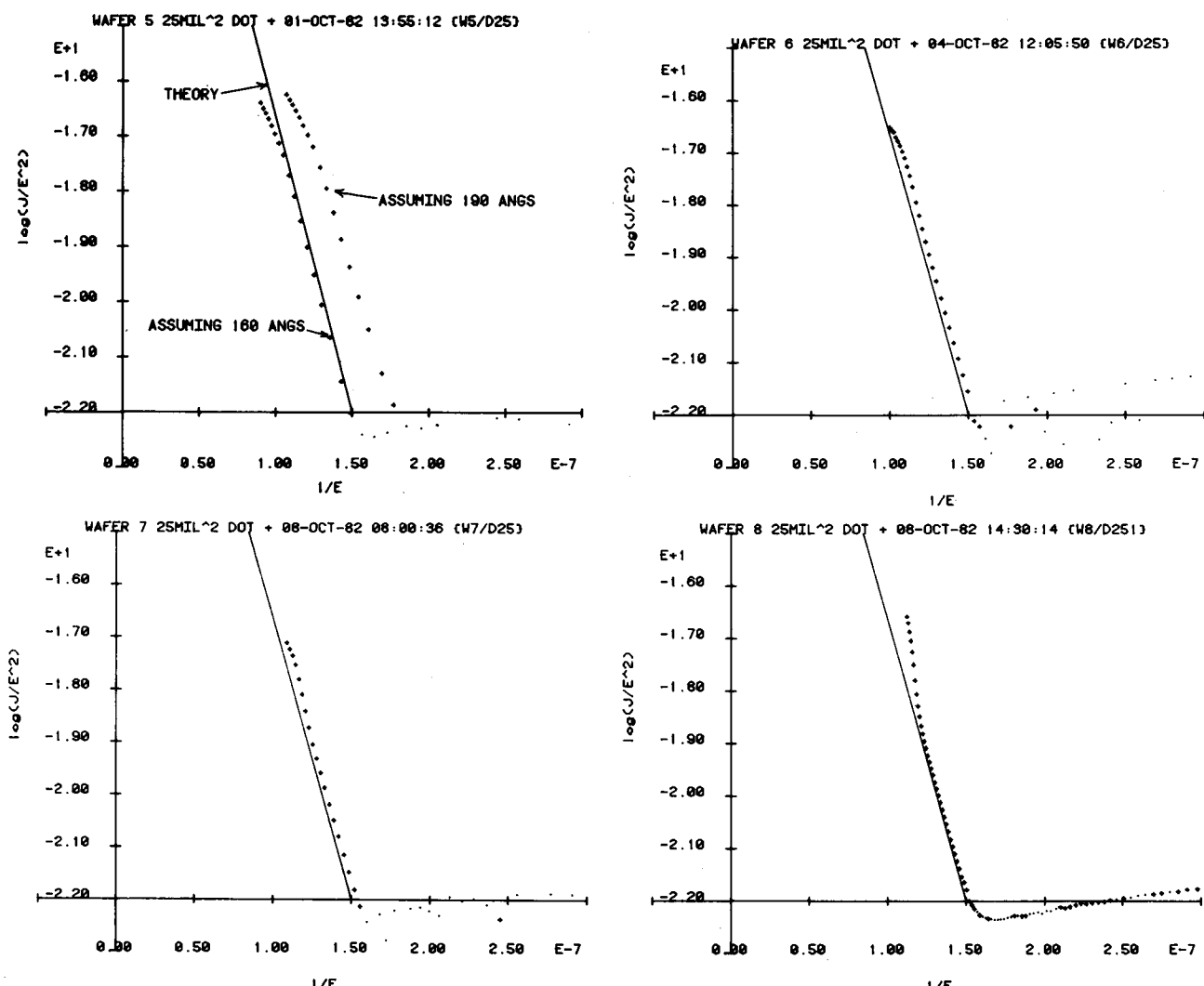


Fig. 4. Fowler-Nordheim plots for injection from silicon for various thicknesses of thermal SiO₂. Theory shown as solid lines. Top left: Wafer 5 assuming $t_{ox} = 160\text{\AA}$ and $t_{ox} = 190\text{\AA}$. Best agreement with theory occurs for $t_{ox} = 160\text{\AA}$. Top right: Wafer 6, 345 Å. Bottom left: Wafer 7, 652 Å. Bottom right: Wafer 8, 1453 Å.

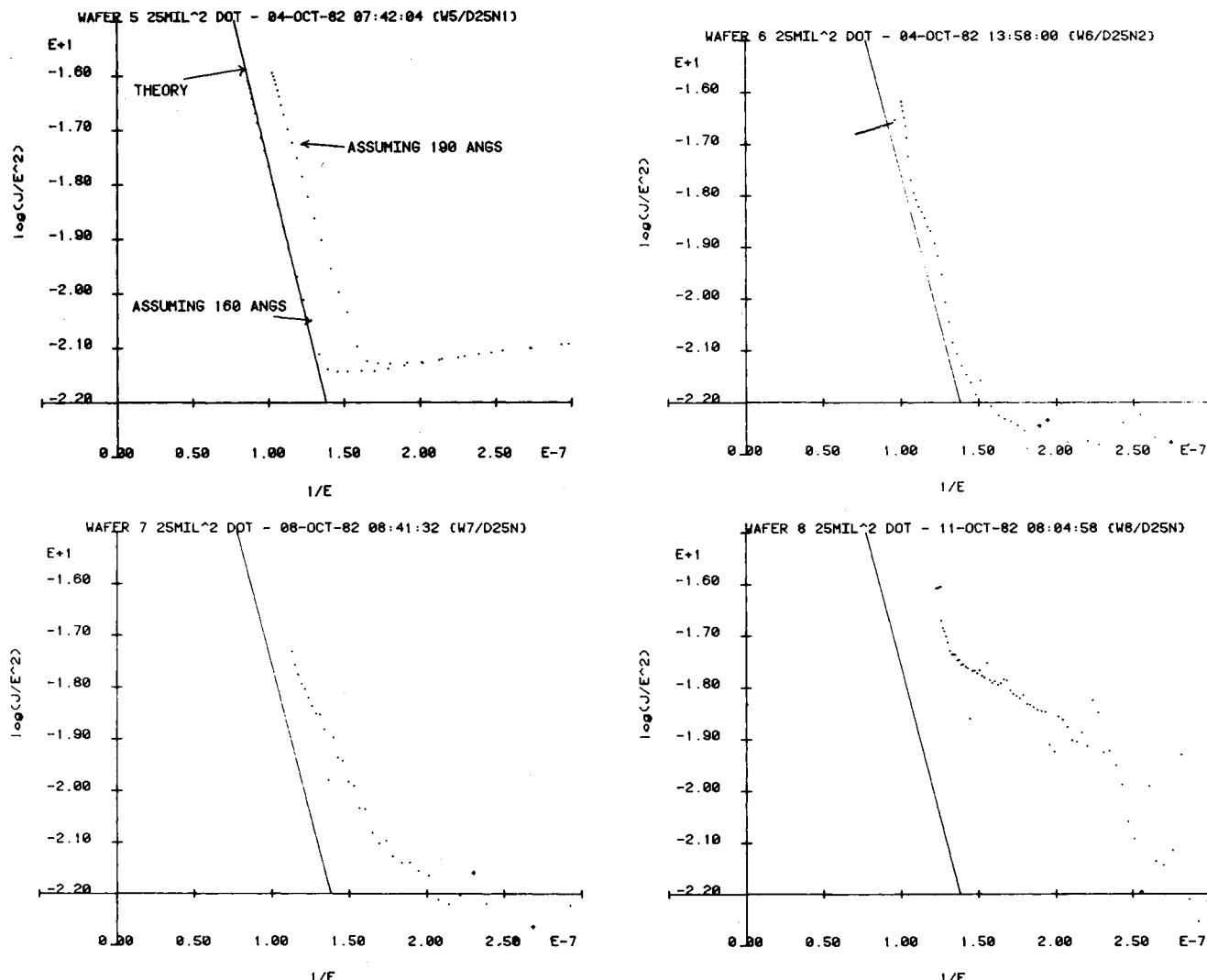


Fig. 5. Fowler-Nordheim plots for injection from aluminum for various thicknesses of thermal SiO₂. Theory shown as solid lines. Top left: Wafer 5 assuming $t_{ox} = 160\text{ \AA}$ and $t_{ox} = 190\text{ \AA}$. Best agreement with theory for $t_{ox} = 160\text{ \AA}$. Top right: Wafer 6, 345\text{ \AA}. Bottom left: Wafer 7, 652\text{ \AA}. Bottom right: Wafer 8, 1453\text{ \AA}.

Al biased positive is plotted with "+" signs, while data with the opposite polarity is plotted with dots. Note also that many of the computer-generated plots have "E + 1" near the end of the x- or y-axis. This means that the appropriate scale numbers are to be multiplied by 10. In general $E + n$ means multiplication by 10^n . The IV characteristic was taken to breakdown so that the smallest value of 1/E on a plot is taken as a measure of (the reciprocal of) the breakdown field, E_b . The same kind of data was obtained for 625 mil² capacitors and identical curves were obtained, except that E_b tended to be lower.

It is valuable to compare our experimental data with theoretical expectations. Fowler-Nordheim tunneling has received considerable attention in the literature over the years (3-5), so that there is now a good consensus of opinion regarding the J-E characteristic for various electrode materials. This is summarized in a recent paper by Weinberg (5). The FN characteristic is

$$J/E_c^2 = C \exp(-\beta/E_c) \quad [1]$$

where E_c is the cathode field, where

$$C = q^3 m / (16\pi^2 \hbar m_{ox} \phi_0) = 1.54 \times 10^{-6} (m/m_{ox}) / \phi_0 \text{ A/V}^2 \quad [2]$$

and

$$\beta = (4/3)(2m_{ox}\phi_0)^{1/2} / (q\hbar) = 6.83 \times 10^7 (m_{ox}/m)^{1/2} \phi_0^{3/2} \text{ V/cm} \quad [3]$$

In Eq. [2] and [3], q is the electronic charge, m is the elec-

tron rest mass, m_{ox} is the electron effective mass in the oxide, \hbar is Planck's constant divided by 2π , and ϕ_0 is the height above the electrode conduction band in electron volts of the barrier at the cathode. It is important to understand that it is the electric field at the electron injecting interface, the cathode, which governs the current density. In Fig. 1, the cathode electric field in the oxide is represented by the slope of the oxide energy bands at the cathode. A consensus of the literature (5) is that $m_{ox} = 0.5m$, $\phi_{Al} = 3.13$ eV, and $\phi_{Si}(100) = 2.96$ eV. The aluminum barrier height is to be used in Eq. [2] and [3] for injection from aluminum, i.e., aluminum biased negative relative to the substrate, while ϕ_{Si} is to be used for aluminum biased positive relative to the substrate. If we assume negligible charge in the oxide, then the cathode field, E_c , equals the average field and we may use Eq. [1] with the consensus parameters to compare the theoretical predictions with our data. This is done by superimposing the theoretical J-E relationship, shown as the solid straight lines, over our data in the FN plots in Fig. 4 and 5.

Corrections were applied to the raw IV data before plotting it in Fig. 4 and 5. The corrections caused an appreciable change from the raw data only for the thinnest oxide; nonetheless, the corrections were applied to all of the data. The measured voltage drop across the MOS diode should be corrected for band bending at the silicon surface and the metal-semiconductor work function difference to give the actual potential drop across the oxide (8). For Al negative, voltage was increased slowly enough that the inversion layer in the silicon always had time to

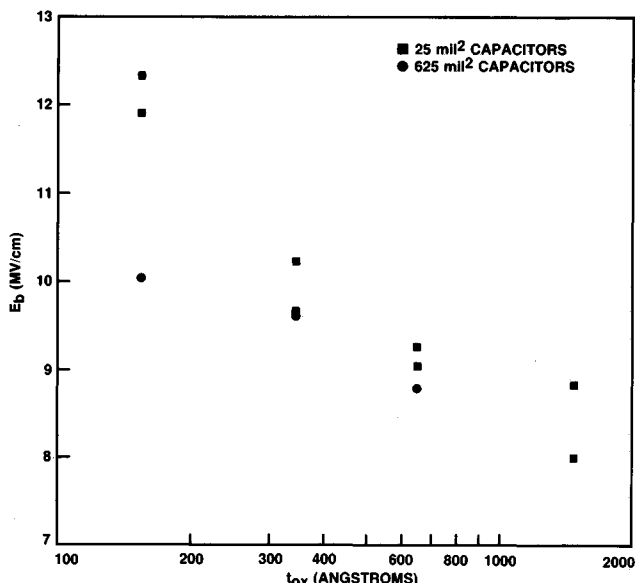


Fig. 6. Breakdown electric field for injection from aluminum. Thermal oxides on n-type silicon (Y58).

form. This means that the usual equilibrium theory (9) may be used to compute these corrections. The corrections amount to about a volt (a bandgap) in inversion, and less in accumulation. This can be an appreciable correction for thin oxides. Specifically, the total potential, V_{TOT} , of aluminum relative to bulk silicon is related to the voltage drop across the oxide, V_{ox} , by

$$V_{TOT} = \phi_{MS} + V_{ox} + \Psi_s(E_s) \quad [4]$$

where $\Psi_s(E_s)$ is the semiconductor surface potential relative to the bulk as a function of the field E_s at the semiconductor surface. E_s is related to V_{ox} by

$$E_s = (K_{ox}/K_s)(V_{ox}/t_{ox}) \quad [5]$$

Equation [4] assumes that there is no charge in the oxide. In strong inversion ($V_{ox} < 0$), we have

$$\Psi_s = -(kT/q) \ln [(E_s^2 K_s \epsilon_0 n)/(2kTn_i)] \quad [6]$$

while in accumulation ($V_{ox} > 0$)

$$\Psi_s = (kT/q) \ln [(E_s^2 K_s \epsilon_0)/(2kTn)] \quad [7]$$

where ϵ_0 is the permittivity of the vacuum, k is

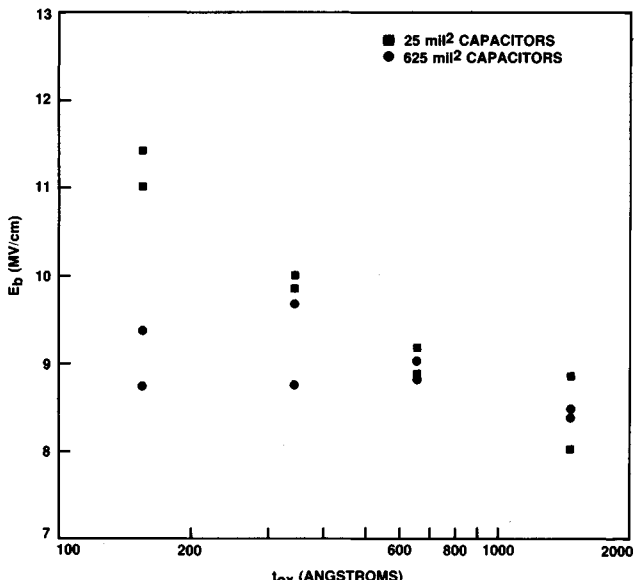


Fig. 7. Breakdown electric field for injection from silicon. Thermal oxides on n-type silicon (Y58).

CV PROCEDURE DEFINITION

OLD PROCEDURE NAME: INJ144N

Step#	1	(Trace)	\$V_{start} = 1.00\$ \$V_{stop} = -1.00\$ \$R = 0.01\$ (V/s) Freq= 1.0E+004 (Hz) \$T = 25.0\$ (deg C)
Step#	2	(Soak)	Time = 10 (sec) Temp= 25.0 (deg C) Bias= -7.20
Step#	3	(Trace)	\$V_{start} = 1.00\$ \$V_{stop} = -1.0\$ \$R = 0.01\$ (V/s) Freq= 1.0E+004 (Hz) \$T = 25.0\$ (deg C)
Step#	4	(Soak)	Time = 10 (sec) Temp= 25.0 (deg C) Bias= -8.64
Step#	5	(Trace)	\$V_{start} = 1.00\$ \$V_{stop} = -1.00\$ \$R = 0.01\$ (V/s) Freq= 1.0E+004 (Hz) \$T = 25.0\$ (deg C)
Step#	6	(Soak)	Time = 10 (sec) Temp= 25.0 (deg C) Bias= -10.08
Step#	7	(Trace)	\$V_{start} = 1.00\$ \$V_{stop} = -1.00\$ \$R = 0.01\$ (V/s) Freq= 1.0E+004 (Hz) \$T = 25.0\$ (deg C)
Step#	8	(Soak)	Time = 10 (sec) Temp= 25.0 (deg C) Bias= -11.52
Step#	9	(Trace)	\$V_{start} = 1.00\$ \$V_{stop} = -1.00\$ \$R = 0.01\$ (V/s) Freq= 1.0E+004 (Hz) \$T = 25.0\$ (deg C)
Step#	10	(Soak)	Time = 10 (sec) Temp= 25.0 (deg C) Bias= -12.96
Step#	11	(Trace)	\$V_{start} = 1.00\$ \$V_{stop} = -1.0\$ \$R = 0.01\$ (V/s) Freq= 1.0E+004 (Hz) \$T = 25.0\$ (deg C)
Step#	12	(Soak)	Time = 10 (sec) Temp= 25.0 (deg C) Bias= -14.40
Step#	13	(Trace)	\$V_{start} = 1.00\$ \$V_{stop} = -1.00\$ \$R = 0.01\$ (V/s) Freq= 1.0E+004 (Hz) \$T = 25.0\$ (deg C)

Fig. 8. A CV procedure typical of those used to produce the data in Fig. 9 and 10. Each trace step is identical. Each soak step is the same except for a linearly increasing stressing electric field.

Boltzmann's constant, q is the electronic charge, T is the absolute temperature, K_{ox} is the oxide dielectric constant, n_i is the intrinsic electron concentration, and n is the bulk electron density. The Eq. [4]-[7] give a relationship between V_{TOT} and V_{ox} . When parameters appropriate to the substrate and metal used in this experiment ($\phi_{MS} = -0.33V$, $n = 5 \times 10^{14} \text{ cm}^{-3}$) are substituted into the equations we find that over the range of voltages for which FN conduction occurs, the difference between V_{ox} and V_{TOT} is practically constant. In accumulation (fortunately), $V_{TOT} = V_{ox}$, while in inversion $V_{TOT} = V_{ox} \times 1.26V$. This holds for all four oxides tested. Thus, in practice only the data for injection from aluminum was corrected. Even with this correction, the thinnest oxide FN data deviated appreciably from theory. It was possible to adjust the assumed thickness of the thinnest oxide upwards by 16 to 160 Å and get excellent agreement with the FN theory simultaneously for injection from Si and from Al². It is known that the IBM FTA tends to underestimate the thickness of thin oxides, so careful ellipsometer measurements were made. With the refractive index forced to $n = 1.465$ (He-Ne laser), a thickness of 190 Å was found. The ellipsometer data were definitely inconsistent with 160 Å and, *a fortiori*, 144 Å, provided $n = 1.465$. On the other hand, 190 Å is inconsistent with the "consensus" parameters in the FN theory, as can be seen in Fig. 4 and 5. Thickness estimates from CV measurements agreed with the ellipsometer estimates. There are several possible explanations for these discrepancies: (i) the refractive index of the oxide is different from the $n = 1.465$ assumed in the

²It is worth noting that simultaneous agreement with theory for both polarities is not possible for any thickness unless the band bending and work-function difference corrections are applied.

ellipsometer calculations. If the refractive index is not forced to a value, then the ellipsometer data give $t_{ox} = 160\text{\AA}$ and $n = 1.8$. (ii) The oxide has a complicated graded optical structure. (iii) The thin oxide has a lower interfacial barrier than the thicker oxides. Adjustment of the barrier heights to give agreement with theory for both polarities assuming $t_{ox} = 190\text{\AA}$ gives $\phi = 2.67 \text{ eV}$. (iv) The electronic effective mass is different for thin oxides or (v) some other reason. We are unable to resolve this discrepancy, but it seems that the IBM FTA reading is definitely low. We shall take 160\AA as the thickness of the thinnest oxide for much of the discussion which follows. The thicker oxides have good agreement with FN theory without any of these corrections. Nonetheless, the band bending and work-function difference corrections were applied to the data for the thicker oxides. This discussion shows that detailed interpretation of thin oxide FN data is considerably more complicated than for thicker oxides.

Several observations can be made from the FN plots in Fig. 4 and 5 and their deviations from theory.

1. For injection from Si, the IV data agree well with FN theory except at high fields just below breakdown. The nature of the deviation at high fields depends on oxide thickness. For the 1453\AA oxide, the data deviate from the FN theory to higher current densities. For the thinnest (160\AA) oxide, the deviation from the FN theory is to lower current densities. For intermediate oxide thicknesses, deviation is first to the high side of the FN curve and then lower as E increases.

2. For injection from aluminum, the current-voltage data agree well with the FN theory only for the thinnest oxide. As the oxides become thicker, the deviation from the FN theory increases, all in the direction of higher current densities. That is, the films are "leakier" than predicted by the FN theory. As the electric field increases,

the IV characteristic for the thicker films approaches the FN curve.

3. The electric field at breakdown as determined from all of the IV data taken is shown as a function of oxide thickness in Fig. 6 and 7. Two main trends are apparent: (i) the well-known increase in breakdown field for decreasing oxide thickness (10), and (ii) the breakdown field for smaller capacitors tends to be higher than for larger capacitors, especially for thinner oxides. The IV characteristics for the large and small area capacitors are in excellent agreement when scaled according to area, but for the larger area capacitors the current density does not reach quite as high a value before breakdown occurs. It is difficult to interpret the area dependence of E_b without sampling a large number of dots to obtain statistical data.

Capacitance-conductance-voltage measurements.—Because the IV data were so reproducible, it was feasible to carry out ac capacitance-conductance-voltage (CGV) measurements on virgin capacitors using stresses comparable with those used in the IV measurements. The CGV data give information on charging and interface state generation which occurs during the conduction process. Two types of CGV data are acquired: (i) data as a function of stress level held for fixed times at each level, and (ii) data as a function of time at a fixed stress.

Isochronal CV data with varying stresses.—The IV traces were examined and a series of stresses extending into the prebreakdown region, but avoiding breakdown, was chosen. The electric fields ranged from 5 MV/cm to 9 or 10 MV/cm in 1 MV/cm steps. An initial CGV trace was taken on a virgin capacitor. Then, an alternating series of stress and trace was carried out with increasing electric field stress but exactly the same trace conditions. Each stress level was held for 10s at room temperature. This

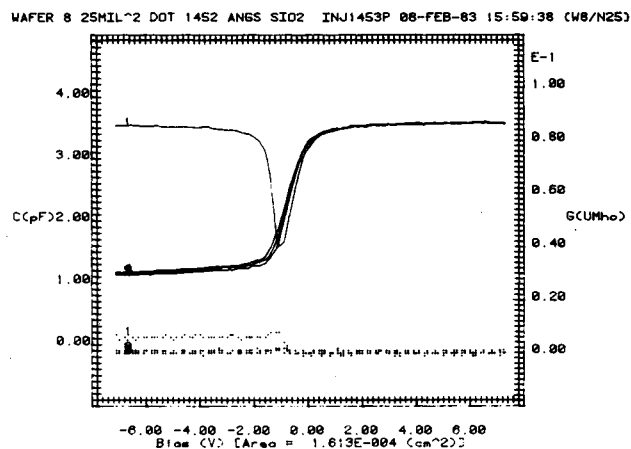
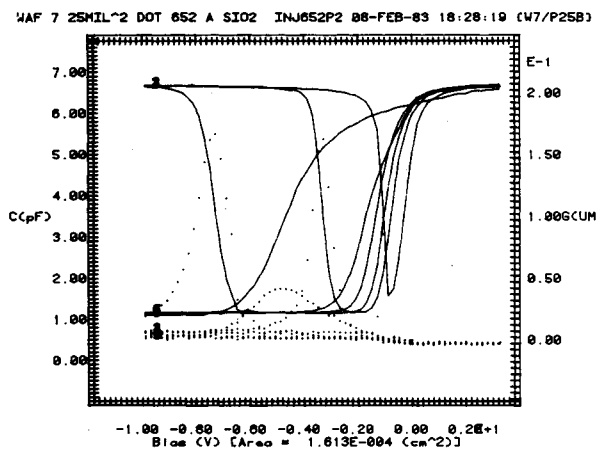
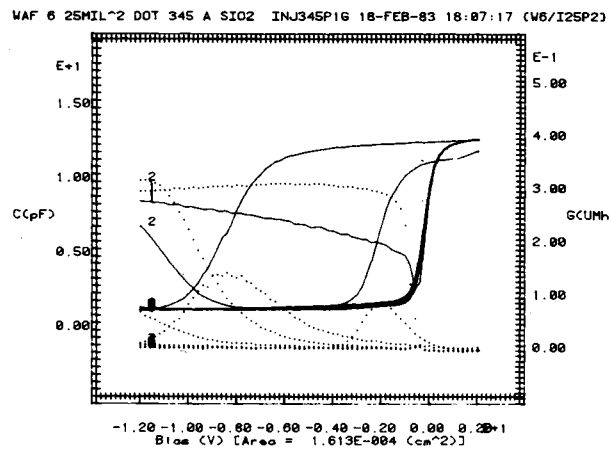
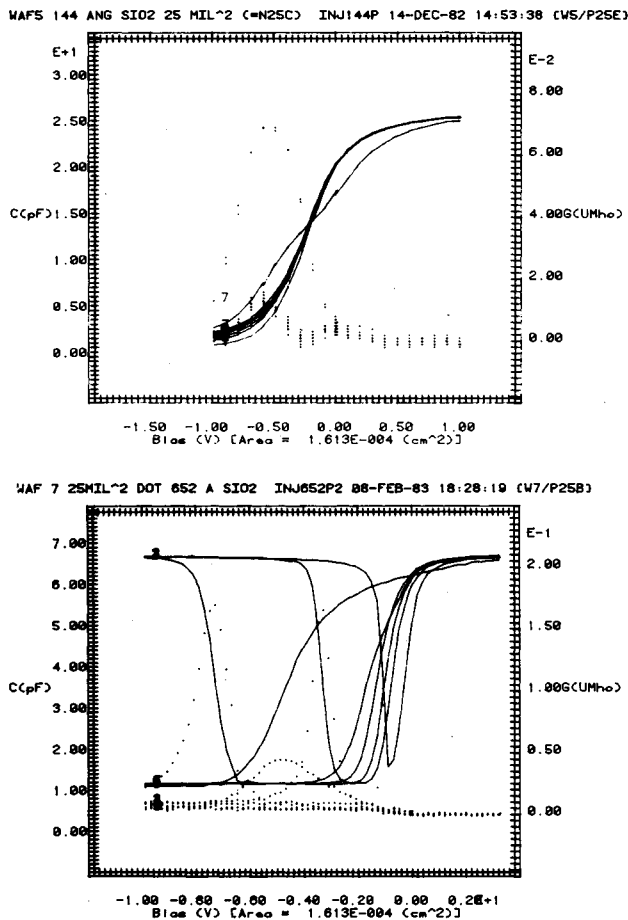


Fig. 9. CV data for injection from Si, i.e., Al was biased positive. Traces were taken at 10 kHz and 25°C . Trace 1 is for the virgin capacitor. Subsequent traces were made after successively higher electric field stresses starting at 5 MV/cm and increasing in steps of 1 MV/cm . Each stress was held for 10s at 25°C .

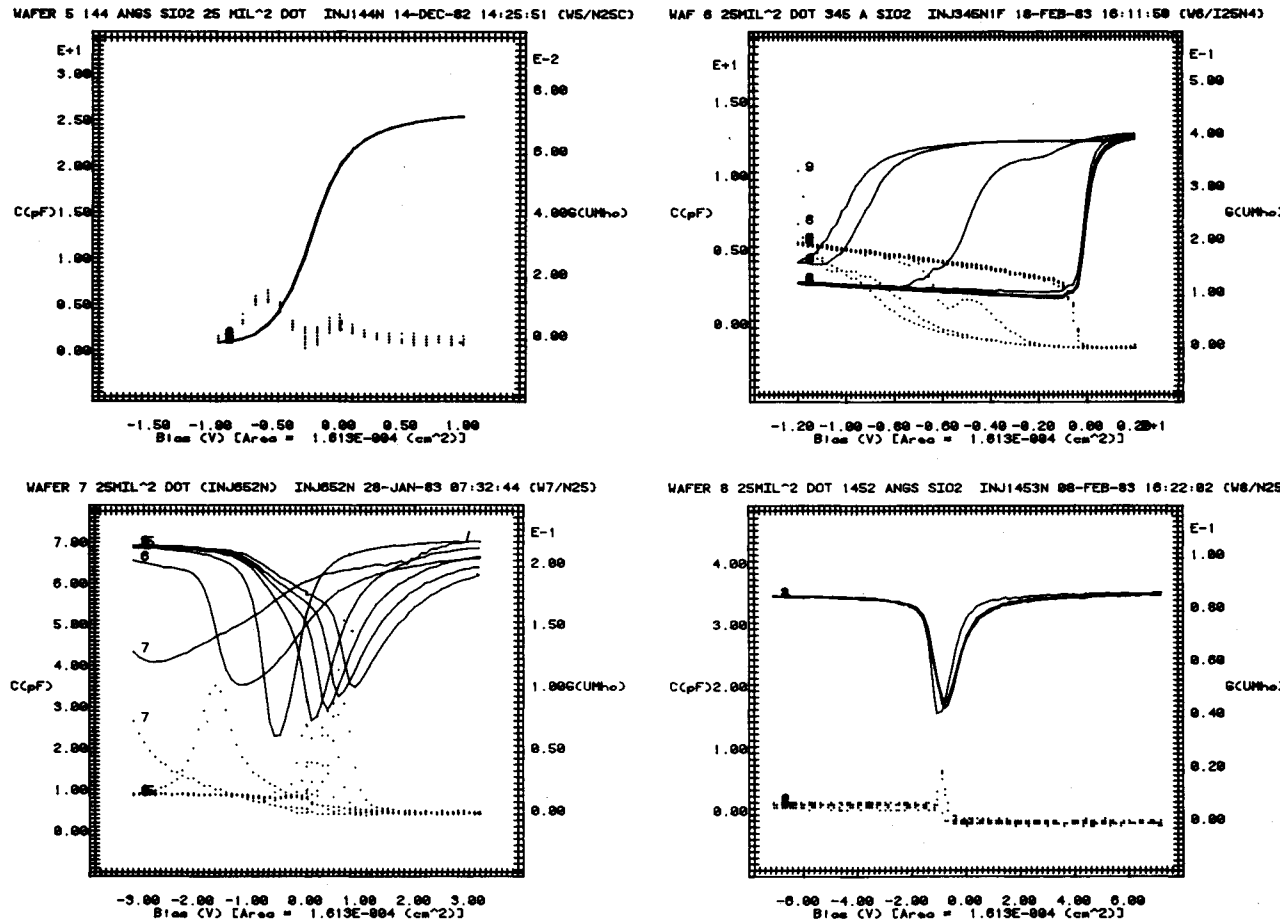


Fig. 10. CV data for injection from Al, i.e., Al was biased negative. Traces were taken at 10 kHz and 25°C. Trace 1 is for the virgin capacitor. Subsequent traces were made after successively higher electric field stress starting at 5 MV/cm and increasing in steps of 1 MV/cm. Each stress was held for 10 s at 25°C.

was done in both polarities. There was insufficient bias capability in our CGV measurement equipment to stress the 1453 Å oxide into the prebreakdown region. The automatic CV system in our laboratory is well suited to this

type of measurement because a complicated sequence may be set up off line and then executed whenever a measurement is needed. The system is described in detail elsewhere (11). A typical procedure definition is shown in Fig. 8.

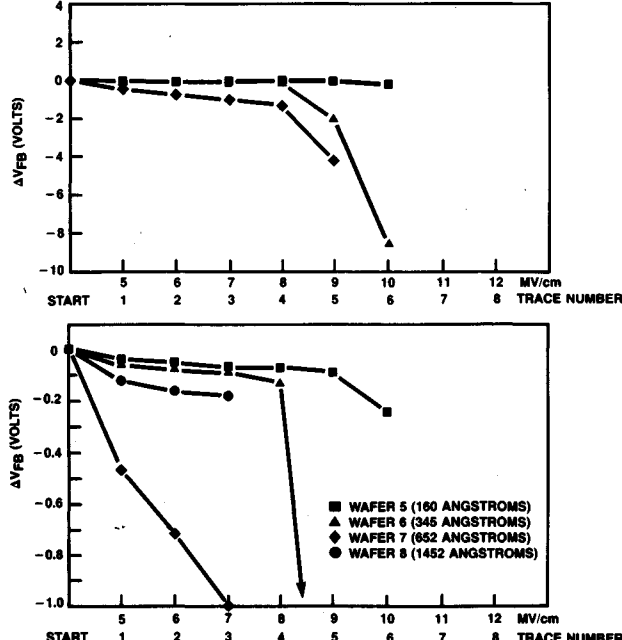


Fig. 11. Cumulative flatband voltage shifts after stress at successively higher electric fields. For injection from silicon. Taken from CV data in Fig. 9. Trace 1 is after 5 MV/cm stress for 10 s, trace 2 is after 6 MV/cm stress for 10 s, etc. Top: all data. Bottom: Expanded voltage scale.

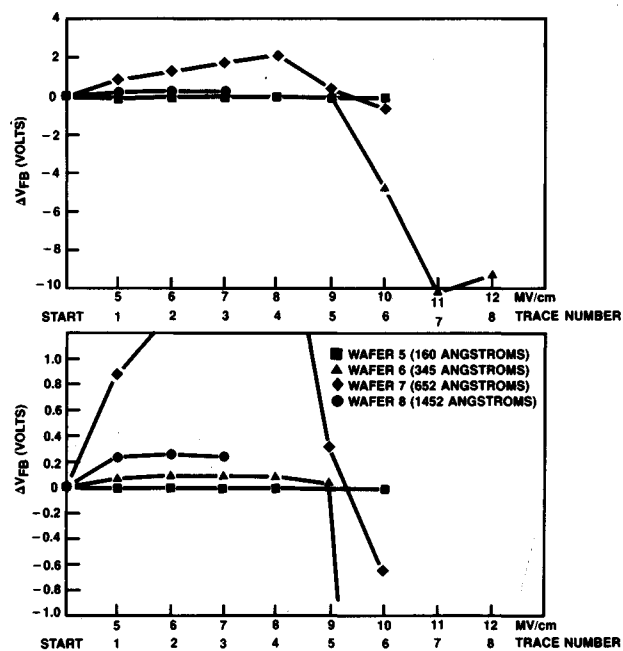


Fig. 12. Cumulative flatband voltage shifts after stress at successively higher electric fields. For injection from aluminum. Taken from CV data in Fig. 10. Trace 1 is after 5 MV/cm stress for 10 s, trace 2 is after 6 MV/cm stress 10 s, etc. Top: All data. Bottom: Expanded voltage scale.

CGV data obtained in this way were quite reproducible. Typical sets of traces are shown in Fig. 9 and 10. Figure 9 shows data for injection from silicon, while Fig. 10 shows data for injection from aluminum. The shifts of the flatband voltage from the flatband voltage of the first trace were obtained from the data of Fig. 9 and 10 and plotted vs. stress level in Fig. 11 for injection from Si and in Fig. 12 for injection from Al. This was done automatically, using a CV analysis utility in the CGV data acquisition system (11). In Fig. 11 and 12, a positive ΔV_{FB} corresponds to a rightward shift of the CV trace and a negative charge in the oxide film. Quantitatively, the relation between ΔV_{FB} and charge induced in the film is

$$\Delta V_{FB} = -\bar{x}Q_{tot}/(\epsilon_0 K_{ox})$$

where Q_{tot} is the total charge induced in the film by the stress which caused the shift and \bar{x} is the location of the centroid of the distribution of the induced charge, measured from the Al/SiO₂ interface. In the following discussion, a flatband shift is interpreted qualitatively as charge in the film, but it must be kept in mind that the magnitude of the shift depends on the position of the charge as well as its magnitude. The data in Fig. 9-12 may be interpreted as follows.

Wafer 5, $t_{ox} = 160\text{\AA}$.—No flatband shifts occur for either polarity, so no charge was induced in the film, except, possibly, close to the Al/SiO₂ interface. For injection from Al no change occurs in the traces. But for injection from Si, the traces become more and more distorted (but unshifted) as the stress increases. The slight shifts shown in

Fig. 11 are just a reflection of the distortion of the traces in Fig. 9, rather than true shifts. Note particularly the large increase in the conductance peak (G) after the final 10 MV/cm pulse. This will be examined in more detail below.

Wafer 6, $t_{ox} = 345\text{\AA}$.—For injection from Si, lower field strengths induce small positive charges until the 9 and 10 MV/cm pulses induce large positive charges. For injection from Al, lower field pulses induce small negative charges, but eventually the 9, 11, and 12 MV/cm produce large positive charges which swamp the earlier-induced negative charge.

Wafer 7, $t_{ox} = 652\text{\AA}$.—Flatband shifts of either polarity were relatively easy to induce. For injection from Si, increasing stress levels induced moderate positive charges until a 9 MV/cm stress caused a large amount of positive charge. For injection from Al, increasing strength pulses cause increasing amounts of negative charge until the 9 and 10 MV/cm pulses reduce the net charge, and even begin to make it positive.

Wafer 8, $t_{ox} = 1453\text{\AA}$.—Slight negative charging occurred for injection from Al, and slight positive charging was seen for injection from Si. High fields could not be obtained because of the limits of our equipment.

CV data as a function of time at a fixed stress level.—A series of CGV measurements was undertaken to measure the accumulated change due to a given stress held for increasing accumulated time. This gives an idea of the times required to produce charging, etc. A trace (or

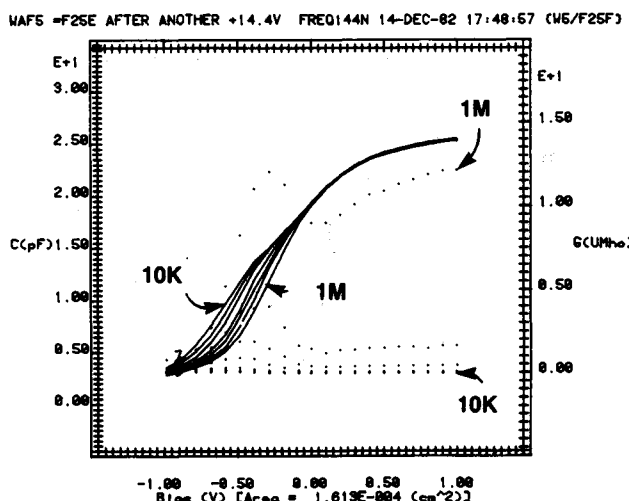
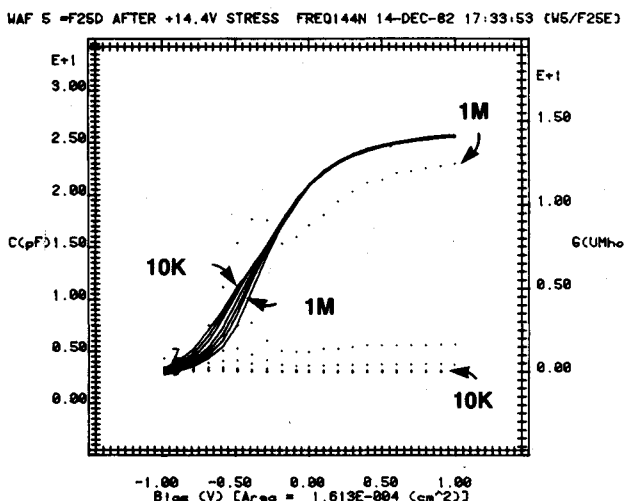
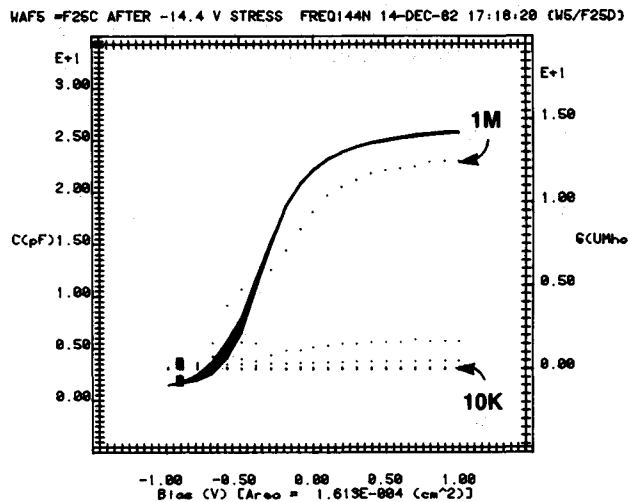
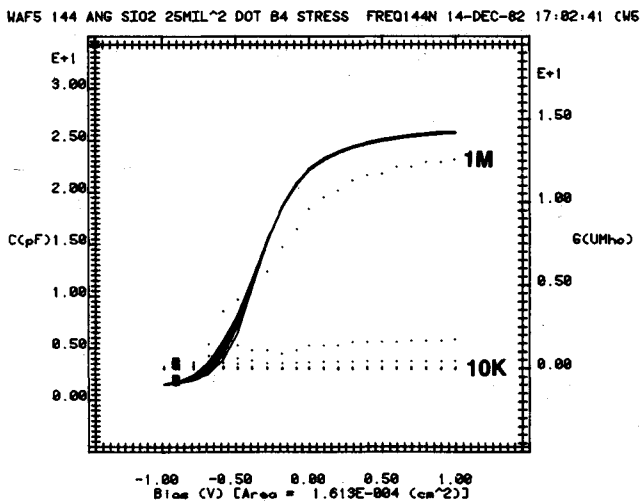


Fig. 13. CGV traces taken at a series of frequencies: 10 kHz, 20 kHz, 40 kHz, 100 kHz, 200 kHz, 400 kHz, and 1 MHz. Dotted lines are G (right-hand scale) and solid lines are C (left-hand scale). All data are taken on the same 25 mil² capacitor. Top left: virgin capacitor. Top right: after 10s of negative (on Al) 10 MV/cm. Bottom left: after a further 10s of positive 10 MV/cm pulse. Bottom right: after another 10s positive 10 MV/cm pulse.

traces) which characterize the oxide were alternated with stresses of fixed duration and voltage. All traces and stresses were done at room temperature.

Wafer 5, $t_{ox} = 160\text{\AA}$.—The changes in the thinnest oxide due to high field stresses show up as distortions in the CGV traces, Fig. 9 and 10 upper left, rather than as flatband shifts. We therefore decided to take a series of traces at different frequencies to display the effect of fast states being created at the injecting interface. In Fig. 13, we show frequency series CGV data. At the top left is the data for a virgin capacitor. After 10s at 10 MV/cm with injection from Al (top right, Fig. 13), there is no discernable change in the CGV characteristics. This capacitor was then stressed for 10s at 10 MV/cm with injection from Si (bottom left, Fig. 13) and distortion of the CV traces at low frequency was seen. Also, the conductance is seen to have a peak in the depletion region of the CGV plots. A further pulse of 10s at 10 MV/cm with injection from Si caused further distortion in the CV plots and further growth of the peak in G (bottom right, Fig. 13). This was repeated with injection from Si four additional times. The distortion of the low frequency C plot increased, as did the peak in G. The conductance data in Fig. 13 are replotted in Fig. 14 as $G/2\pi f$ vs. $\log f$ (f = frequency) with bias as a parameter. The density of interface traps, N_{it} , is proportional to $G/2\pi f$ (12). An increase in N_{it} causes a proportional increase in $G/2\pi f$. We have taken the height of the envelope of curves at 100 kHz in Fig. 14 as a measure of N_{it} in arbitrary units. In Fig. 15, we have plotted N_{it} in these arbitrary units after each of the pulses described above. It is clear from Fig. 15 that injection from Al causes no increase in the fast states at the Si/SiO₂ interface. However, injection from Si causes increases in N_{it}

which are beginning to saturate after about 60s of accumulated injection at 10 MV/cm. Another measurement was made in which a positive 10s, 10 MV/cm pulse was the first stress on a virgin capacitor. The increase in N_{it} due to this is also shown in Fig. 15. This demonstrates reproducibility and that injection from Al in the first series had no effect on subsequent developments, owing to injection from Si.

Wafer 6, $t_{ox} = 345\text{\AA}$ and wafer 7, $t_{ox} = 652\text{\AA}$.—For these wafers, the main effect of the stress in the prebreakdown region is to shift the flatband voltages. For both wafers, single 10 kHz CGV traces alternated with room temperature stresses. Each stress was held for 2s. The electric field was 10 MV/cm for wafer 6 and 9 MV/cm for wafer 7 since 10 MV/cm caused breakdown of the oxide on wafer 7. The results are shown in Fig. 16. Careful comparison reveals that the results of Fig. 16 are consistent with those of Fig. 11 and 12. We could not produce fields in the prebreakdown region of wafer 8 with our CV equipment. Therefore, there are no data for the time dependence of the flatband voltage for the thickest oxide.

For wafer 6, positive charge generation reaches a limit after 6s of injection from Si at 10 MV/cm. The time to reach the steady-state flatband shift is considerably slower (10s) for wafer 6 when injection is from Al, but the final flatband shift is the same whichever electrode is injecting.

An electric field of 9 MV/cm for injection from Al on wafer 7 does not seem to be enough to create any positive charge, but it does seem to be sufficient to detract any electrons (negative charge) trapped at lower fields. This seems to be true for all the oxides because all of the curves in Fig. 12 cross the X-axis near 9 MV/cm. Figure

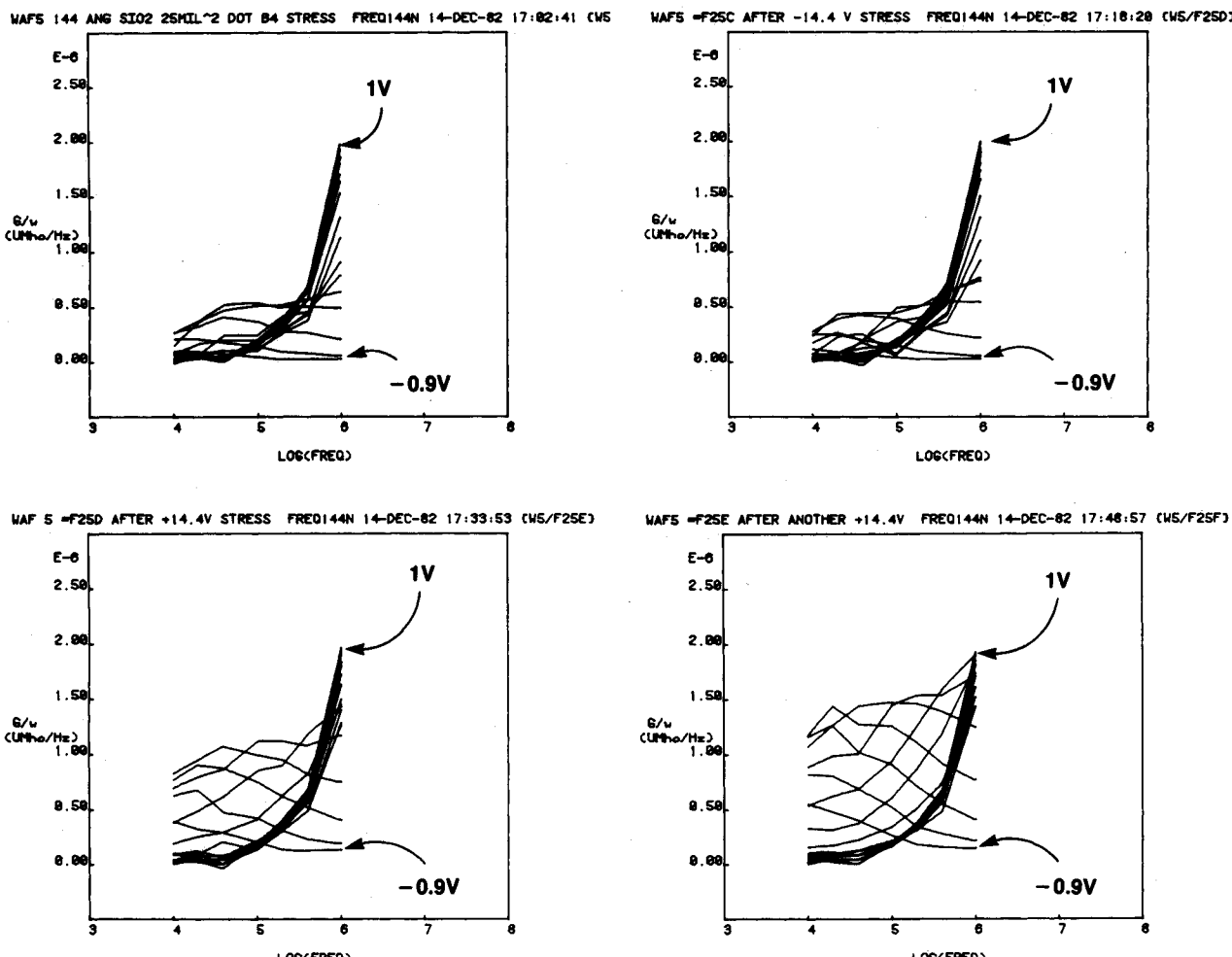


Fig. 14. GV data from Fig. 13 replotted as $G/2\pi f$ vs. $\log f$ (f = frequency) with bias as a parameter. The curves are plotted at 0.1V intervals for biases ranging from -1 to 1V.

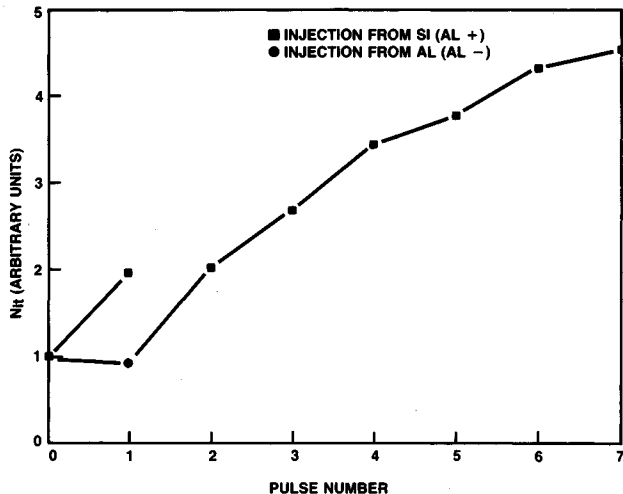


Fig. 15. The effect of high electric-field charge injection on N_{it} . For wafer 5: n-type (Y58), $t_{ox} = 160\text{\AA}$, capacitor area = 25 mil². Pulse width = 10s, pulse height = 10 MV/cm.

16, bottom, shows that this condition can be maintained as a steady state. Injection from Si induces positive charges at lower fields than injection from Al, as can be seen from Fig. 11 and 12. Thus, for wafer 7, injection from Si at 9 MV/cm caused considerable positive charging within 2s, whereas injection from Al at the same field caused none (Fig. 16, bottom). The cause of the slow relaxation in the flatband voltage after 2s in Fig. 16, bottom, is not known.

Constant-current V-t characteristics.—The last set of data obtained was the voltage-time characteristic of a virgin test capacitor into which a constant current was forced. The characteristic is obtained by simultaneously unshorting the capacitor, redirecting a current from a constant-current supply onto the capacitor, triggering a high speed DVM, and monitoring the voltage across the capacitor as a function of time. At first, the voltage increase is linear with time as the test capacitor (and stray capacitance) charges. Eventually, conduction through the dielectric becomes appreciable, and the voltage is determined by the IV characteristic of the capacitor and by the current being forced. The voltage in this condition is constant if the IV characteristic of the capacitor does not change. However, space-charge buildup in the dielectric changes the IV characteristic and hence V, so the shape of the V-t characteristic in the conduction regime gives information on charging of the dielectric. This type of information, coupled with simultaneous flatband shift measurements, has been used by Meyer and Crook (16) to characterize trapping in thin oxides. We studied only injection from Si since this maintains the substrate in accumulation, thus avoiding the problem of accounting for the voltage drop across the depletion layer.

Examples of the data obtained for three thicknesses and three current densities are shown in Fig. 17. Several observations can be made: (i) the thicker oxides have an initial peak, whereas this is absent in the thinnest oxide, (ii) the initial peak, when it occurs, is sharper for higher current densities, (iii) all oxide thicknesses show a slow increase in voltage; this occurs after the initial peak for the thicker oxides, but starts immediately for the thinnest oxide, (iv) the slow increase in V is more rapid at higher current densities, and (v) not shown in Fig. 17 is the considerable scatter in time to breakdown, making generalization about times to breakdown difficult without better statistics. Still, the thinnest oxide seemed to have longer times to failure than the thicker oxides.

Discussion

The electrical results described in the previous section can be interpreted in terms of the band diagrams in Fig. 18. These diagrams incorporate the ideas of Harari (6, 7), Solomon (15), Shatzkes and Av-Ron (8), and DiStefano

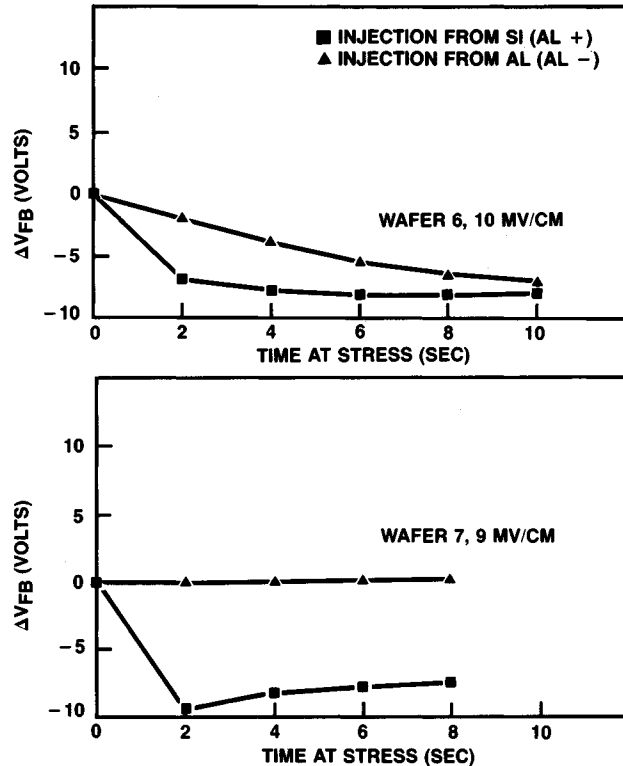


Fig. 16. Accumulated flatband voltage shifts vs. accumulated time at stress for wafer 6 ($t_{ox} = 345\text{\AA}$) and wafer 7 ($t_{ox} = 652\text{\AA}$). Stress was 10 MV/cm for wafer 6 and 9 MV/cm for wafer 7.

and Shatzkes (14). The diagrams are drawn for the case of a constant cathode field, that is, when a constant current is forced into the oxide and for high fields near breakdown. The time evolution of these bands is shown for thin oxides (6, 7, 16) and thick oxides (8, 14). Electrons injected from an electrode are accelerated by the internal field in the oxide and are scattered, forming a Poisson-shaped energy distribution which broadens and moves to lower energies as distance from the cathode increases. An electron in a part of this distribution which lies above the ionization threshold can create an electron-hole pair. The ionization threshold is one bandgap potential above the oxide conduction band. This is shown as dotted lines in Fig. 18. For thick oxides or high average fields, the peak in the hot electron distribution rises above the ionization threshold somewhere in the oxide causing ionization. The electrons so formed become part of the hot electron distribution, but the holes have very low mobility and so are practically fixed in position. For thin oxides or low average fields, there is insufficient distance or field strength to accelerate the hot electrons to a kinetic energy above the ionization threshold anywhere in the oxide, so no holes are formed. We shall call an oxide "thin" if a field high enough to cause impact ionization cannot be reached before the oxide breaks down. Thus there are two distinct types of behavior depending on oxide thickness. Oxides thinner than 250-300 \AA will never show a positive charge buildup due to immobile holes, whereas thicker oxides will.

The band diagrams in Fig. 18 can be used to interpret the V-t characteristics in Fig. 17 for injection from Si. The cathode field, that is, the slope of the bands at the cathode, is fixed by the current density being forced. The forced current density and the cathode field are related by the FN law. For thin oxide, traps near the cathode are generated and filled with electrons (6, 7, 15). This causes a downward bending of the oxide bands to the right of the trapped electrons (see Fig. 18). As trap creation and filling proceeds, this bending continues and causes the voltage difference across the capacitor to increase. This effect is seen for the 160 \AA oxide in Fig. 17. Eventually, breakdown occurs when the electric field exceeds some

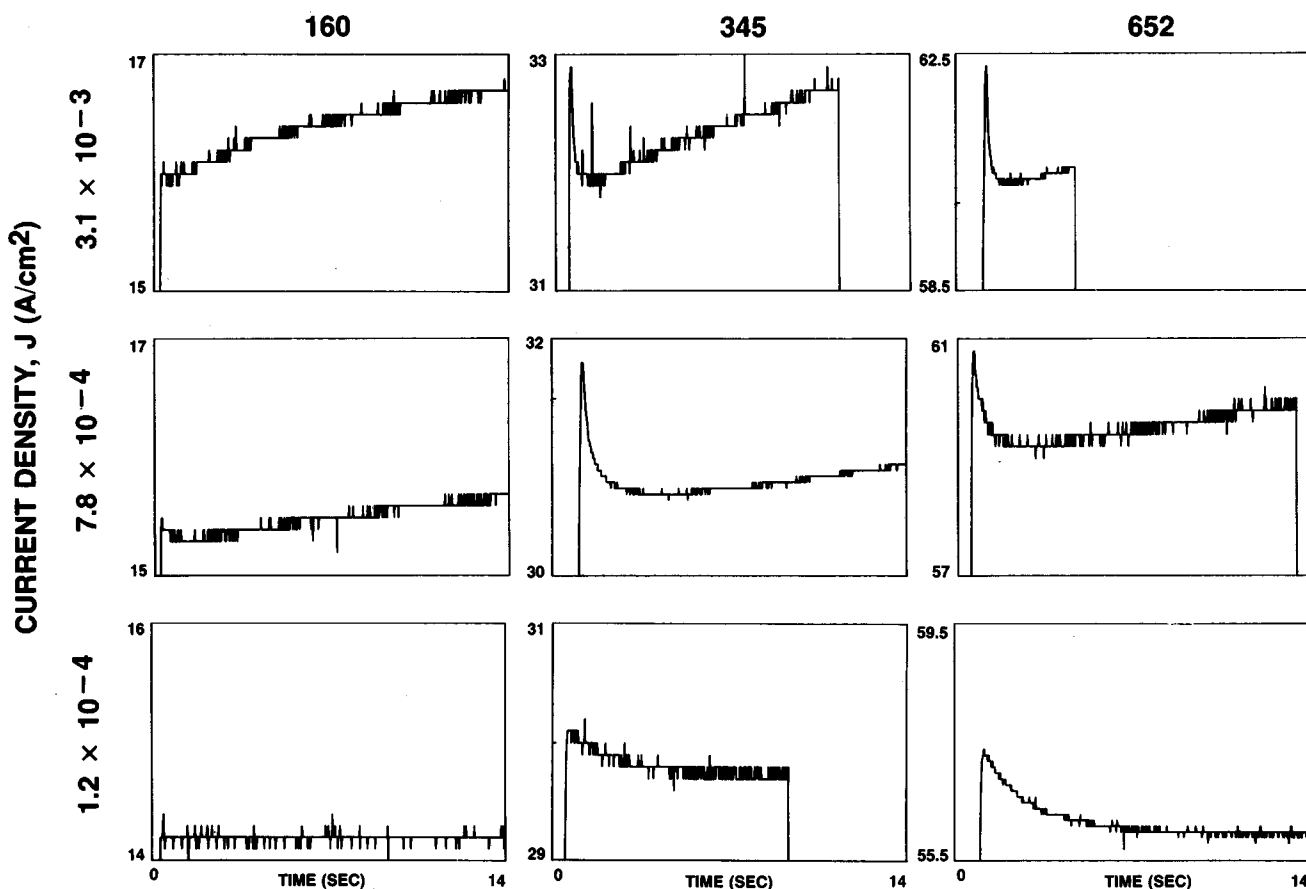
OXIDE THICKNESS, t_{ox} (Angs.)

Fig. 17. Forced-current voltage-time characteristics for three oxide thicknesses (columns) and three current densities (rows). All data are for injection from silicon. Horizontal (time) axes are the same for all plots. Voltage range is shown on vertical axes.

critical value somewhere in the oxide, variously estimated as 30 MV/cm (7), 11.2 MV/cm (16), etc. For thick oxide, a relatively rapidly formed positive charge due to holes generated by ionization reduces the voltage drop across the oxide from its initial value (see Fig. 18). This is the origin of the initial peak in the V-t characteristic for the thicker oxides. After this initial formation of positive charge, electron traps are generated and filled near the cathode, just as for the thin oxide, causing a slow rise in the voltage drop across the oxide (see Fig. 17). Both the positive charge and the negative charge build up more rapidly for higher current densities.

The effects of hole formation deep in the oxide and trap formation and filling near the cathode also show up in the IV and CV data. For the moment, our discussion is confined to injection from Si. The IV and CV data were taken under forced voltage, not forced current, conditions so the illustration in Fig. 18 does not strictly apply. For the thinnest oxide, the buildup of negative trapped charge at the cathode under fixed voltage conditions reduces the cathode field below the measured average field and hence reduces the injected current. This explains the deviation to lower current densities from the FN law observed in the thinnest oxide (see Fig. 4). However, for the thicker oxides, the rapid buildup of positive charge causes an enhancement of the cathode field above the average field, increasing the current above the FN prediction. Eventually, the slow buildup of trapped negative charge near the cathode tends to reduce the cathode field again bringing current back to the FN prediction, or lower. Thus the same mechanisms explain both the V-t characteristics in Fig. 17 and the deviations from the FN law observed in Fig. 4. The difference is that one characteristic is observed under forced current conditions, while the other is observed under forced voltage conditions.

The CV characteristics for injection from Si, Fig. 11, show only negative flatband shifts. That is, they show

only the positive charge induced in the thicker oxides. In the CV traces for the thinnest oxide, there is no sign of the negative charge which was observed in the IV and V-t characteristics. It seems that the traps created and filled with electrons during stress discharge when the stress is removed to make a CV trace. This means that they must be very close to the injecting interface and are in electrical communication with the bulk Si. Thus, at least some of the traps observed in the IV and V-t data are the interface traps detected in the frequency CV data in Fig. 13-15. The conductance-voltage traces for the thicker oxides (Fig. 9) also show peaks which increase in height with increasing stress, thus showing the formation of interface traps. The CGV data are therefore entirely consistent with the IV and V-t data if the negatively charged traps near the injecting interface are understood to be interface traps which discharge (but do not heal) when stress is removed.

The IV characteristics for injection from aluminum were "leakier" than the FN theory, except for the thinnest oxide (see Fig. 5). This may be due to degradation of the Al/SiO₂ interface by a chemical reaction. The increasing deviation from the FN theory as the oxide thickness increases is not understood. When the cathode field is large enough to cause appreciable charge injection through an ideal triangular barrier by the FN mechanism, the electric fields in the bulk of the oxide are large enough to cause immediate detrapping by tunneling out of the numerous grown-in traps at about 2 eV below the oxide conduction band. Thus, no charging of these grown-in traps will occur. The grown-in traps are distributed uniformly throughout the bulk of the oxide and are to be distinguished from the current-induced interface traps described above. However, if the interface is a more efficient injector than a simple triangular tunneling barrier, then large numbers of electrons will enter the oxide and fill traps at fields low enough that detrapping will not

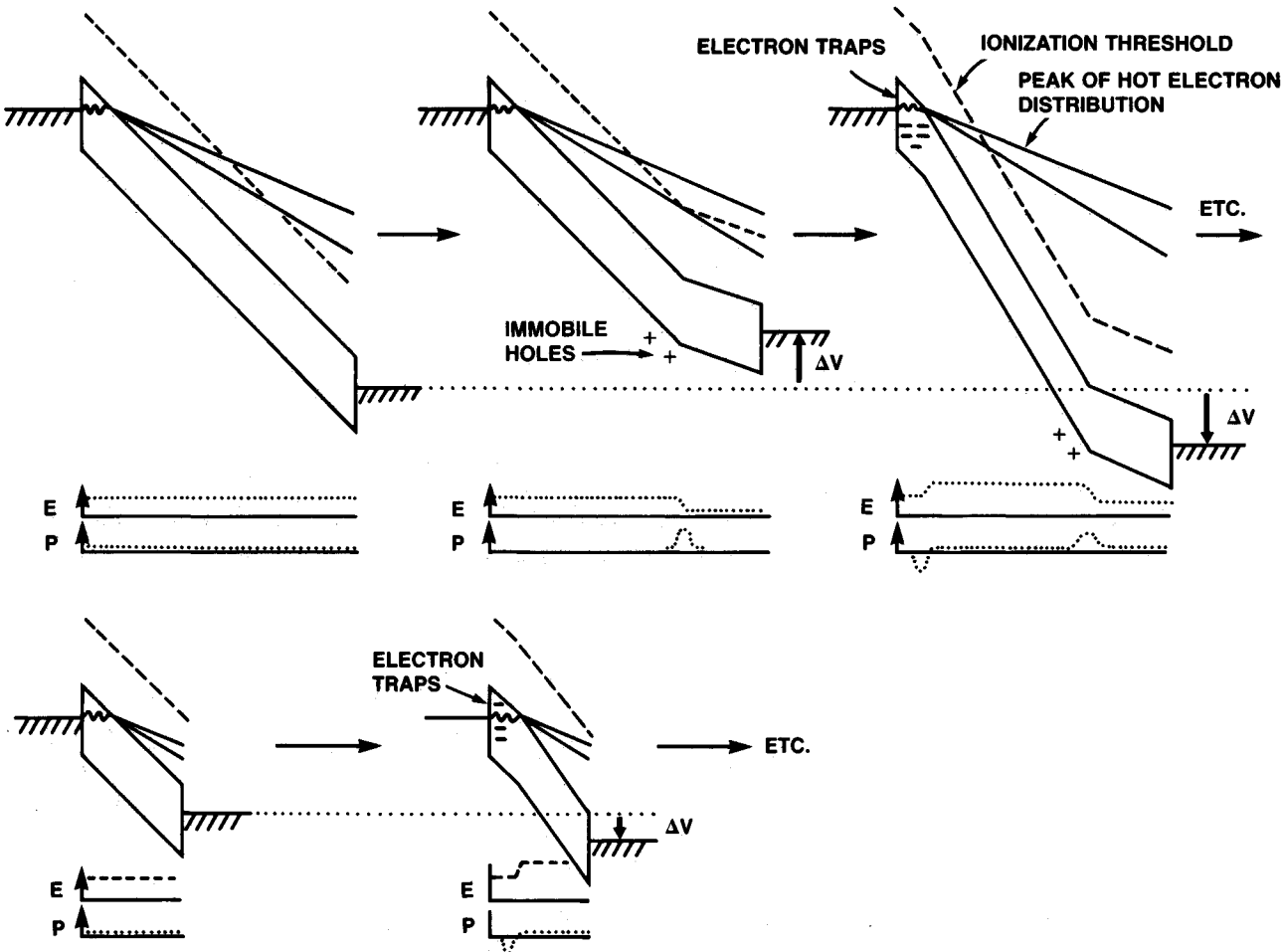


Fig. 18. Time evolution of bands, electric fields, and charges for thick oxide (top) and thin oxide (bottom). Drawn for constant forced current

occur (20). Thus, the negative charging evidenced by the positive flatband shifts shown in Fig. 12 is probably due to bulk trapping and is consistent with the "leakier" than FN current-voltage characteristics in Fig. 5. Notice that the thinnest oxide, which obeys the FN law, shows no evidence of bulk trapping. As the electric field increases the IV characteristics approach the FN characteristic (Fig. 5), bulk traps are emptied, and impact ionization produces holes which produce negative flatband shifts (Fig. 12).

This discussion has shown that all of the data can be explained in terms of a simple model with the following features: (i) impact ionization produces immobile holes in thicker oxides, (ii) interfacial trap formation and filling near the cathode occur in all of the oxides, and (iii) for "leaky" interfaces, such as the Al/SiO₂ interface in our particular oxides, bulk trapping occurs. These charges distort the bands in the oxide and create internal electric fields which differ from the average electric field. Whenever the electric field somewhere in the oxide exceeds a critical value, breakdown occurs. At a given average electric field, the relative rates of generation of charge formation by the above three mechanisms, especially the first two, determine the time to breakdown. Defects, weak or thin spots in the oxide, etc., will all contribute to a scatter in the times to breakdown. Another factor which determines the time to breakdown is the way in which the oxide is stressed: *viz*, by forced current or forced voltage, the rate of charge buildup is different for each of these methods.

Conclusions

We have presented a qualitative picture of high field trapping and ionization phenomena in thermal oxides as a function of oxide film thickness. This was done by integrating three types of data: (i) IV data, (ii) CV data,

and (iii) forced-current voltage-time data. Interface trap formation and charging with electrons near the cathode during injection from Si was observed for all oxides. Creation of immobile holes in the oxide valence band by impact ionization was observed for the thicker oxides, but not the thinnest. Bulk trapping was significant when electrons were injected from Al into the thicker oxides. For the thicker oxides, the Al/SiO₂ interface was considerably leakier than predicted by the FN theory. This type of measurement is an important adjunct to long term reliability studies since these phenomena cause wear-out of intrinsic oxides.

There is still considerable controversy as to exactly what mechanisms occur in oxides at highfields (16-19). We have interpreted our data according to what seem to be the most likely mechanisms (7, 8, 15). A partial reason for many of the conflicting observations in the literature must be differences, documented and otherwise, in the processes which produce MOS test capacitors. This shows the importance of setting up the techniques described in this report as a process-development tool as opposed to making the measurements once with the hope of pinning down the mechanisms once and for all. Measurement techniques set up as a process-development tool must be highly automatic both in data acquisition and data analysis in order to facilitate throughput.

Most of the analysis in this report has been qualitative because our purpose has been to review and illustrate rather than to make a detailed quantitative analysis of a particular oxide. Still, it is clear that quantitative analysis such as calculation of cross sections, trapping efficiencies, etc., are quite straightforward since all the data are stored in digital form on floppy disks, and are easily accessible for computer analysis.

The discussion has shown the power of using multiple techniques in unraveling mechanisms. For example, the

CV shifts due to bulk trapping when electron injection was from aluminum would have been difficult to understand without the FN data. It is also worth emphasizing the value of FN data by itself as an analytical tool, especially when comparison is made with theoretical expectations. FN analysis is not as widely recognized as a process development tool as is, say, CV measurement.

Acknowledgments

Thanks are due to the following individuals: C. E. Wu for helpful discussions, Rick Cosway for supplying oxides, Kathy Ginn for processing, Dan McGuire for help with measurements, and Sue Trower for typing this paper.

Manuscript received Dec. 21, 1983.

Motorola, Incorporated, assisted in meeting the publication costs of this article.

REFERENCES

1. D. J. DiMaria, in "The Physics of SiO₂ and Its Interfaces," Pergamon Press, New York (1978).
2. H. F. Wolf, "Semiconductors," Interscience, New York (1971).
3. M. Lenzlinger and E. H. Snow, *J. Appl. Phys.*, **40**, 278 (1969).
4. C. M. Osburn and E. J. Weitzman, *This Journal*, **119**, 603 (1972).
5. Z. A. Weinberg, *J. Appl. Phys.*, **53**, 5052 (1982).
6. E. Harari, *Appl. Phys. Lett.*, **30**, 601 (1977).
7. E. Harair, *J. Appl. Phys.*, **49**, 2478 (1978).
8. M. Shatzkes and M. Av-Ron, *ibid.*, **47**, 3192 (1976).
9. S. M. Sze, "Physics of Semiconductor Devices," Wiley-Interscience, New York (1969).
10. C. M. Osburn and D. W. Ormond, *This Journal*, **119**, 597 (1972).
11. C. G. Shirley, *Semicond. Intl.*, **5**, 81 (1982).
12. E. H. Nicollian, A. Goetzberger, and A. D. Lopez, *Solid State Electron.*, **12**, 937 (1969).
13. C. M. Osburn and N. J. Chou, *This Journal*, **120**, 1377 (1973).
14. T. H. DiStefano and M. Shatzkes, *J. Vac. Sci. Technol.*, **12**, 37 (1975).
15. P. Solomon, *J. Appl. Phys.*, **48**, 3843 (1977).
16. W. K. Meyer and D. L. Crook, Paper presented at the International Reliability Physics Symposium, Phoenix, AZ (1983).
17. C. S. Jenq, T. R. Raganth, C. H. Huang, H. S. Jones, and T. T. L. Chang, *IEDM*, 388 (1981).
18. M. S. Liang and C. Hu, *ibid.*, 396 (1981).
19. M. Itsumi, *J. Appl. Phys.*, **52**, 3491 (1981).
20. D. J. DiMaria and D. W. Dong, *ibid.*, **51**, 2722 (1980).